Cobalt Iron Oxides Prepared by Acidic Redox-assisted Precipitation: Characterization, Applications and New Opportunities

Chia-Hao Yeh,[a] Wan-Yun Hsu,[a] Chun-Cheng Hsu,[a] Joey Andrew A. Valinton,[a] Chen-I Yang,[b] Cheng-chau Chiu*[a] and Chun-Hu Chen*[a]

[a]Department of Chemistry, National Sun Yat-sen University

Kaohsiung 80424, Taiwan

[b]Department of Chemistry, Tunghai University

Taichung 40704, Taiwan

*Corresponding author, email address: ccchiu@mail.nsysu.edu.tw; chunhu.chen@mail.nsysu.edu.tw; tel.: 886-7-525-2000 ext. 3943; fax: 886-7-525-3908

Abstract

Microscopic homogeneity of mixed metals in a single-phase oxide is a critical issue on improving material performance. Aqueous alkaline precipitation is the most common approach, but has the limits of microscopic inhomogeneity due to intrinsically different precipitation rates between metal cations. Herein, we demonstrate a new preparation of uniformly structural substituted cobalt iron oxides via acidic redox-assisted precipitation (ARP) upon the interaction of Co^{II} and K_2FeO_4. This low-pH synthesis features the redox process between Co and Fe, presumably through the formation of inner-sphere complexes (such as $[(H_2O)_5Co^{II}\text{-}O\text{-}Fe^{VI}O_3]$). With the nucleation starting from such complexes, one obtains a product with predominantly mixed-metal Co-O-Fe moieties, which improves the electrical conductivity of the product. This work further analyzes how the properties of the product species evolve during the hydrothermal synthesis step in the ARP process. We see that the Co/Fe ratio slowly increases from about 1:1 to a final value of 2:1, but does not reach the expected redox stoichiometry of 3:1. At the same time, the magnetization also increases, reaching a value of 16.9 $emu \bullet g^{-1}$ for the final superparamagnetic product, which is three times higher than the value of monometallic Co_3O_4 and Fe_2O_3. The cobalt iron oxide samples obtained from ARP also possess superior oxygen evolution activity (307 mV) overpotential (at 10 $mA \bullet cm^{-2} \bullet \mu g^{-1}$) compared to a mixture of Co_3O_4 and Fe_2O_3 (422 mV) or pure cobalt oxide (350 mV), highlighting the structure-induced enhancement of the catalytic activity. The difficult synthesis of evenly blended trinary/quaternary metals in a single oxide phase may become possible in future via ARP.

Keywords: acidic redox-assisted precipitation, potassium ferrate, multi-metal oxides, oxygen evolution, superparamagnetism

1. Introduction

Spontaneous and simple aqueous-phase synthesis of multinary transition metal oxides which feature long-range, metal-oxygen backbones with alternative metals is promising breakthrough of novel multi-functional semiconductors.[1-3] Polarized electron structures resulting from inequivalent electron-attraction between different metal cations, generally enhance catalytic reactivities, conductivity, and magnetic behaviors. Aside from that, this feature provides the opportunity of band gap engineering, which is valuable for photo-assisted chemistry, light-emission technology, and semiconductor devices/sensors.[4-7] Multinary metal oxides are promising in enabling highly-selective tandem reactions due to the presence of multiple reaction centers.[8-10] By incorporating more than two homogeneously distributed metals in an amorphous oxidic structure, one can obtain so-called high entropy oxides[3,11,12] which can be potentially simplified by aqueous-based deposition.

Protocols for the preparation of multinary transition metal oxides in literature are mostly based on alkaline precipitation, a well-known approach in textbooks.[13] Typically, bases (e.g. NaOH, NH_4OH, urea, etc.) are added in an aqueous dispersion containing the target metal cations to yield metal hydroxide precipitates, which are then calcined in an subsequent step to obtain oxides. Typically, such synthesis strategies do not involve changes in the oxidation states of the involved metal ions. One disadvantage of the alkaline precipitation is that the prepared products may show microscopically inhomogeneous metal distributions. This is a consequence of deviating solubility product constants K_{sp} for the involved transition metal cations, which causes different precipitation rates.[14,15]

Therefore, precipitation based on direct metal-to-metal interactions, rather than metal-to-hydroxide ion reaction, is a straightforward solution to address this issue. In the previous studies, aqueous redox reactions between low-valent metal cations (as reductants) and potassium permanganate (as metal-containing oxidant), have successfully generated precipitates of multinary oxides under acidic conditions.[4,15-17] The redox process tends to create structures featuring mix-valency and structural vacant sites with different elemental compositions, which are highly desired to achieve versatile catalytic activities in a broad range of applications.[6,14,18-26] Although there are only few reports on this synthesis strategy referred to as "acidic redox-assisted precipitation" (ARP), it represents a rising alternative to alkaline precipitation.

Potassium permanganate is probably the mostly used metal-containing oxidant in the literature to perform ARP. This is likely due to the well-balanced aqueous stability, which avoids self-decomposition in water, and its relatively strong oxidizing capability compared to, for example, K_2CrO_4 or $K_2Cr_2O_7$.[4,19,22] Oxidants with too weak oxidizing potentials cannot react with metal cations that have stable electron configurations (e.g. Ni^{II}, Cu^{II}, etc.).[27-30] We thus attempt to explore new oxidants with even higher oxidizing potentials than $KMnO_4$ while maintaining a reasonable aqueous stability. One of the stronger oxidation agents that is known for low biological/environmental impacts is potassium ferrate (VI), K_2FeO_4. Despite that, potassium ferrate (VI) has not been explored yet as a candidate for ARP.[31] No knowledge of redox reactions between K_2FeO_4 and other transition metal cations to yield multinary metal oxides has been systematically reported.

In this work we conducted ARP using potassium ferrate (VI) and Co^{II} in low-pH aqueous conditions to yield cobalt iron oxides (CFO). We found interesting that the Co/Fe ratio in

the products change, up to a certain boundary value, with the initial precursor ratio and the reaction time. To our surprise, the Co/Fe ratio does not reflect expected redox stoichiometry, as observed for reactions with $KMnO_4$.[14] The varying Co/Fe ratio allows the preparation of a large variety of compounds with different structural doping as well as different behaviors in magnetism, conductivity, (electro-)catalytic activity, suitable for different applications. In this work we also identify the possible intermediates with experimental and computational methods, in order to propose a possible mechanism for this unique nucleation process.

2. Results

2.1. Material Synthesis

The acidic redox-assisted precipitation (ARP) between $Co(OAc)_2$ and K_2FeO_4 produces binary cobalt iron oxides via an one-step procedure, in which an aqueous solution of the precursor species is heated at 140°C for 12 hours. A small amount of acid was added to keep the pH values in the range of 5.10-5.70 to avoid occurrence of alkaline precipitation (see the detailed synthetic procedure in the Supporting Information). During the synthesis Co^{II} is oxidized to Co^{III} while Fe^{VI} is reduced to Fe^{III}, yielding a deep brown precipitate. This redox reaction is suggested as the following:

$$3Co^{II} + Fe^{VI} \rightarrow 3Co^{III} + Fe^{III} \quad (1)$$

Eq. 1 suggests an ideal redox stoichiometry of Co/Fe=3/1. This ratio was adopted as the typical precursor ratio in the preparation of this study, unless otherwise stated. Thus the CFO sample prepared according to the standard procedure will also be referred to as $CFO_{3/1}$ to reflect the precursor ratio. The XPS data of the ARP products confirm the trivalent state of both Fe and Co, as discussed in Section 2.2. (Fig. S2). To confirm that the synthesis of the CFO really proceeds via a redox step, we compared the products synthesized using K_2FeO_4 (as oxidant) to those using non-oxidizing Fe sources like $FeCl_3$ and $Fe(NO_3)_3$. The XRD results of the as-yielded precipitates (Fig. 1a) show that the product obtained with K_2FeO_4 is a mixed Co_3O_4 spinel phase, while the reactions with $FeCl_3$ or $Fe(NO_3)_3$ yield an Fe_2O_3 phase. In addition, ICP-MS have been used to determine the Co/Fe ratio of the precipitates. One also sees here that the composition of the

precipitates obtained with different Fe precursors is very different: Co/Fe = 1.15:1 (K_2FeO_4), 0.07:1 ($Fe(NO_3)_3$), and 0.06:1 ($FeCl_3$). The latter two cases have significantly lower cobalt contents and product yields, indicating no appreciable interaction between cobalt and iron during the reaction. As such, the intensive interaction of Co^{II} with Fe^{VI} species has been recognized, while there is very weak interaction between Co^{II} and Fe^{III} from $Fe(NO_3)_3$ or $FeCl_3$). This reveals the essential role of the redox reaction in the precipitate formation. Thus, the binary cobalt iron oxides (CFO) is recognized to follow the ARP principle.

We have further prepared two control samples following the same procedure, but adding only K_2FeO_4 or only $Co(OAc)_2$. These samples are referred to as $CFO_{Co\text{-}free}$ and $CFO_{Fe\text{-}free}$, respectively. These control samples are used for characteristic comparison with the CFO (XRD, SEM, FTIR, Raman, and OER). The XRD patterns of $CFO_{Fe\text{-}free}$ correspond to Co_3O_4 phase, while those of $CFO_{Co\text{-}free}$ correspond to Fe_2O_3 phase (Fig. S3).

2.2. XPS Spectroscopy

XPS spectroscopy of $CFO_{3/1}$ shows a binding energy of 799.8 eV for the Co $3p_{3/2}$ state (Fig. S2a), which corresponds to Co^{III} species. In addition, the absence of a satellite at around 785.5 eV confirms that there is no Co^{II} in our sample[32]. The Fe $2p_{3/2}$ signal appearing at 711.0 eV indicates the presence of Fe^{III} species in an octahedral environment (Fig. S2b).[33] All the XPS data well support that the precipitate formation indeed involves the changes in oxidation states as indicated by Eq. 1.

The tetrahedral sites of the spinel Co_3O_4 phase are typically occupied by divalent Co^{II}, while the trivalent Co^{III} occupies the octahedral sites. In our CFO samples, only

trivalent metal ions are present (either Co^{III} or/and Fe^{III}), thus the tetrahedral sites should also be occupied by trivalent metal ions. The octahedral occupancy by trivalent cation remains the same as a typical spinel, according to the XRD data.To balance of the charges in the oxide framework, an exchange mechanism as shown below should be involved, where the total numbers of charges and occupation sites of metal cations should be identical on the both side of equation (Eq. 2):

$$2M^{III}_{Td} + \square_{Td} \leftrightarrow 3M^{II}_{Td} \quad (2)$$

where $\square_{Td}$ is a tetrahedral vacancy. By having trivalent metal ions in the tetrahedral sites of spinel Co_3O_4, every third tetrahedral site should remain unoccupied. As this vacant site was constructed to compensate for the charge, these sites can also be interpreted as defect sites[18].

2.3. Thermal Stability

Thermogravimetric analysis (TGA) was conducted to evaluate the thermal stability of CFO samples under nitrogen atmosphere. As shown in Fig. 1b, $CFO_{3/1}$ and $CFO_{Fe\text{-}free}$ show the desorption of physisorbed gaseous species and water at temperatures below 250ºC.[34,35] At around 250ºC-350ºC, all the samples undergo a second-stage mass loss due to the breaking of chemically-bonded hydroxyls.[34] At these temperatures, $CFO_{3/1}$ lost 8% of its mass which is higher than the loss of $CFO_{Fe\text{-}free}$ and $CFO_{Co\text{-}free}$ at 5%. This can be due to the vacancy sites in the CFO structure as discussed in Section 2.2. These sites feature un-bonded oxygen atoms that tend to form chemically-bonded hydroxyls. Among the three

considered samples, only $CFO_{Fe\text{-}free}$ shows a third stage mass loss at 720ºC, which corresponds to the transformation of Co_3O_4 to CoO.[36] For $CFO_{3/1}$, this transformation is not observed. This is consistent with reports arguing that hindered ion diffusion is the main reason why such a transformation is not observed for iron-doped cobalt oxides.[37]

2.4. Morphology and Conductivity

The SEM images of the $CFO_{3/1}$ sample assemblies that are several micrometers large. The assemblies are composed of fine particles with a diameter of 18 nm (Fig. 2c,d). We also acquired the SEM images of a $^{1h}CFO_{3/1}$ sample that, different to the preparation of the standard sample, has only been heated for one hour. The corresponding image shows the particulate product featuring a smooth surface (Fig. 2a, b). This suggests that there is a transformation from a bulk, continuous chunk into fine nanoparticles over the 12 hours heating during the synthesis.

To confirm that the ARP of Co^{II} species with K_2FeO_4 really leads to the formation of a structure that is different from Co_3O_4 and Fe_2O_3. We have also measured the electrical conductivity of the intermediates formed during the synthesis. Other than in the standard synthesis protocol, we have prepared a $CFO_{3/1}$ sample alongside two control samples Co_3O_4 ($CFO_{Fe\text{-}free}$) and Fe_2O_3 ($CFO_{Co\text{-}free}$) by performing the hydrothermal synthesis step for only 1 h. These samples will be indicated with a "1h" superscript in this work. It can be seen from Table 1 that the conductivity of $^{1h}CFO_{3/1}$ is one and three orders higher than the control samples of Co_3O_4 ($^{1h}CFO_{Fe\text{-}free}$) and Fe_2O_3 ($^{1h}CFO_{Co\text{-}free}$), respectively. To confirm that the $^{1h}CFO_{3/1}$ sample is not just a mixture of the two monometallic oxides, we have also compared it against a physical mixture of the two control samples, which also

features a lower conductivity. This result confirms that already at the early stage of the ARP process, the Fe and Co start to interact with each other and prepare the way for the formation of the CFO which has different characteristics that the corresponding monometallic oxides. The selection of one hour is to confirm that the conductivity variation starts at the early stage of synthesis, rather than at the end of 12 hours preparation. With the further comparison between 1 hour and 12 hour samples (i.e. $^{1h}CFO_{3/1}$ and $^{12h}CFO_{3/1}$), these two samples show similar values in sheet resistance, showing that the intrinsic conductivity enhancement of CFO samples is more likely to be ARP-dependent, rather than strong correlation with reaction time or crystal phase evolution.

2.5. Effect of precursor ratios

A series of precipitates have been prepared with varied Co/Fe precursor ratios, i.e. 10/1, 6/1, 3/1, 1/1, and 1/3. The corresponding samples, following the example of $CFO_{3/1}$ are referred to as CFO_x with x being the precursor ratio. For the samples with a Co/Fe precursor ratio of 1/1 or higher, the XRD results (Fig. 3a) all indicate the presence of a crystalline phase of spinel Co_3O_4, which features a similar XRD pattern as iron-doped Co_3O_4 (i.e. $CoFe_2O_4$) reported in the literature[38]. In the case of $CFO_{1/3}$, the product is characterized as a hematite Fe_2O_3 phase, which probably is due to the elevated Fe content in the precursor. Overall, no impure or mixed phases were observed in all the XRD data, indicating that ARP is capable of yielding binary oxides without impure phases, even if the ratio of the different elements in the precursor strongly deviates from assumed ideal stoichiometry shown in Eq. 1. One interesting issue is the position of the (311) peak in Fig. 3b, which has been assigned following the assignment in JCPDS no. of 01-1152. For Co/Fe

precursor ratio between 3/1 and 10/1, the signal shifts towards higher 2θ values with increasing Co/Fe ratio, which agrees well with literature reports and reconfirms the structural substitution of Fe in the Co_3O_4 phase.[38.39] The Co:Fe mole ratios (ICP-MS analysis) of these samples are 1.61:1 ($CFO_{6/1}$), 1.67:1 ($FCFO_{3/1}$), 0.5:1 (CFO1/1), and 0.29:1 ($CFO_{1/3}$). The relative cobalt contents mostly follow the trend of precursor ratios, but notice that $CFO_{6/1}$ and $CFO_{3/1}$ show the similar values and will be discussed below.

2.6. Infrared and Raman Spectroscopy

To determine the conformational changes in the local environments of Co and Fe in the oxide framework, the CFO samples were investigated with both infrared and Raman spectroscopy. $CFO_{Co\text{-}free}$ shows the peaks at 440 (*v1*-Fe) and 523 cm^{-1} (*v2*-Fe) which are assigned to the Fe-O vibrations typical for a hematite Fe_2O_3 phase (Fig. 4a).[40] At variance, $CFO_{Fe\text{-}free}$ shows the peaks at 557 (*v*1-Co) and 659 cm^{-1} (*v*2-Co). In literature, these two signals are discussed to be associated with the BOB_3 and ABO_3 vibrations, respectively, where A and B represent Co cation in tetrahedral and octahedral coordination geometry in Co_3O_4, respectively.[41,42] The comparison of the infrared spectra of $CFO_{Fe\text{-}free}$, $CFO_{6/1}$, and $CFO_{3/1}$ shows the presence of iron results in a red shift of both *v1*-Co and *v2*-Co, which has been discussed to be a result of a slight distortion of the CoO_6 octahedra caused by the presence of FeO_6.[43] This, in return, suggests the preferential formation of mixed-metal moieties Co-O-Fe in the metal-oxygen backbone over single-metal moieties like Co-O-Co or Fe-O-Fe,[18,44] which is in line with the XRD and conductivity measurements. At higher Fe contents, e.g. in the $CFO_{1/1}$ sample, the *v2*-Co signal is not observed, which indicates a negligible occupancy of the T_d sites by Co^{III}. This suggests that Co prefers to occupy the

octahedral sites first when there is a shortage of Co. The T_d sites are only getting occupied, when the Co content in the precursor surpasses a critical value.

In the Raman measurements (Fig. 4b), the synthesized CFO samples show high similarities to $CFO_{Fe\text{-}free}$. The broad peak at 685.8 cm^{-1} is assigned to the A_{1g} mode associated with the vibrations of the T_d-coordinated CoO_4 sites in the spinel structure.[45,46] The band at 685.8 cm^{-1} remains unchanged upon varying the Co/Fe precursor ratio, which suggests that only cobalt but no Fe is occupying the T_d sites. The bands at around 500 and 350 cm^{-1} correspond to the E_g and T_{2g} modes of the O_h-coordinated MO_6 sites in the spinel structure[45-47]. The E_g band shifted from 492 ($CFO_{6/1}$) to 478 cm^{-1} ($CFO_{1/1}$) upon increasing Fe content (Note: for the straightforward comparison, the swap of E_g and T_{2g} assignment reported in iron-rich spinel oxide, such as $CoFe_2O_4$[47] has been ignored). At the same time, a shift of the T_{2g} peak from 350 ($CFO_{6/1}$) to 340 cm^{-1} ($CFO_{1/1}$) could also be observed. The dependency of these signals on the Co/Fe ratio reveal that both Co and Fe occupy the O_h sites. Thus, both IR and Raman results indicate the predominance of Co-O-Fe mixed-metal moieties in the oxide framework, where only Co^{III} occupies the T_d sites, and the O_h sites are occupied by both Co^{III} and Fe^{III}.

2.7. OER performance

The enhanced conductivity and polarized electronic structures at the active sites, both resulting from the homogeneous distribution of Co and Fe in the CFO sample, have been discussed to be beneficial for the electrocatalytic oxygen evolution reaction (OER).[36] The comparison of the linear scan voltammetry curves (Fig. 5a) obtained for $CFO_{Fe\text{-}free}$ and $CFO_{Co\text{-}free}$ shows that the former, i.e. Co_3O_4, features a much higher catalytic activity than

the latter, Fe_2O_3. According to the LSV data normalized by the cobalt content, $CFO_{3/1}$, with 0.63 mole fraction of cobalt, exhibits an overpotential of η = 336 mV (10 mA•cm^{-2}µg^{-1}), and thus slightly outperforms $CFO_{Fe\text{-}free}$ with a value of 350 mV. We further prepared a sample referred to as $CFO_{physmix}$ by physically blending $CFO_{Fe\text{-}free}$ and $CFO_{Co\text{-}free}$, so it features the same Co/Fe ratio as the $CFO_{3/1}$ sample. It could be shown that the $CFO_{physmix}$ is, with η = 422 mV, even catalytically less active than pure cobalt oxide. This highlights the advantage of the homogeneous metal distribution in the catalyst[48] achieved via ARP and the resulting improved conductivity. The presence of the uniformly substituted iron atoms and maybe also of the defect sites, may have a synergistic effect on the local environment of the Co atoms which results in higher catalytic activities than for pure cobalt oxide.

In addition, we have also performed the OER experiment using the $CFO_{6/1}$, which features a similar Co mole fraction of 0.62 to $CFO_{3/1}$. To our surprise, $CFO_{6/1}$ features an even higher OER activity as indicated by the overpotential of η = 307 mV. Moreover, $CFO_{6/1}$ has exhibited superior OER kinetics to the other samples indicated by the smallest Tafel slope of 69.51 mV•dec^{-1} (Fig. 5b), as well as high stability though maintaining a stable current at 10 mA•cm^{-2} for 6 hours with negligible decay (Fig. 5c). Despite the similar Co/Fe ratio, $CFO_{3/1}$ and $CFO_{6/1}$ show some differences in their structure, as indicated by the XRD results (Figure 3) and the vibrational spectroscopy data (Figure 4). These may come from the occupation of the T_d sites by Co^{III}, which only occurs at higher Co/Fe precursor ratios, as mentioned in Section 2.6.[46] It seems that these differences are playing a role for the catalytic activity, which is unique when compared to the reported electrocatalysts synthesized by conventional alkaline precipitation and others in Table S1.

The inset in Fig. 5a shows that the current density measured for $CFO_{Fe\text{-}free}$ features two peaks at around 1.1 and 1.3 V which corresponds to the $Co^{II/III}$ (peak α) and $Co^{III/IV}$ (peak β) transitions, respectively.[49] The oxidation transition associated with these two peaks is confirmed by the cyclic voltammetry (CV) data for $Co(OH)_2$ shown in Fig. 5d. When performing the CV measurement with $CFO_{6/1}$, the $Co^{II/III}$ transition is not observed (Fig. 5d). This means that the ARP process completely converts Co^{II} to Co^{III}. Since OER activation occurs at a higher potential than the $Co^{III/IV}$ transition (Fig. 5a),[50] the Co^{III} centers in the CFO samples only need to undergo one transition step. In contrast, the Co centers in Co_3O_4 are subject to both $Co^{II/III}$ and $Co^{III/IV}$ transitions. This effect may lower the activation potentials for the CFO samples and lead to a higher activity compared to Co_3O_4 ($CFO_{Fe\text{-}free}$).

Under anodic OER conditions, surface reconstruction of CFO is expected.[51,52] Thus, the changes on the surface were monitored through operando Raman spectroscopy. According to the Raman data of $CFO_{6/1}$ at dry conditions (before immersion into the alkaline electrolyte, see Fig. 5e) indicate the typical CFO peaks at 497, 532, and 699 cm^{-1}, which corresponds to E_g, F_{2g}, and A_{1g} vibrations, respectively, of spinel Co_3O_4.[46] When the catalyst is immersed in the alkaline electrolyte solution (denoted as wet in Fig. 5e), an additional bumpy peak at 615 cm^{-1} becomes visible, which pertains to A_{1g} vibrations of the Co-O bond in $Co^{III}OOH$.[53-55] Moreover, $Co^{III}OOH$ signals at 506 cm^{-1} and 547 cm^{-1} overlap with the E_g and F_{2g} signals in the CFO spinel.[54,55] The presence of both the CFO spinel and the $Co^{III}OOH$ peaks suggest that hydroxylation on the surface layer of CFO, agreeing with the earlier observation.[34] Under the operation beyond the OER activation (at 1.64 V), the

peak at 615 cm^{-1} becomes more prominent, indicating higher degree of surface reconstruction to $Co^{III}OOH$.

2.8. Product structure evolution during synthesis

To understand the CFO formation process, we have varied the heating time during the synthesis and monitored the evolution of the product composition. For these studies, the Co/Fe precursor ratio is kept at 3/1. We will use the labels "$^{t}CFO_{3/1}$" as a shorthand notation to refer to the different samples, with t being the time of the hydrothermal synthesis step. The XRD data of $CFO_{3/1}$ obtained with varying heating times shows that a layered structure of a CoOOH phase is formed during the first hour of the hydrothermal synthesis step at 140°C. That CoOOH phase then transformed into the spinel Co_3O_4 phase over the 3rd to 12th hour of the hydrothermal synthesis (Fig. 6a). On the other hand, the Co/Fe ratio in the synthesized product as characterized by ICP continuously rises from 1.04 in $^{1h}CFO_{3/1}$, to 1.67 in $^{12h}CFO_{3/1}$ (Fig. 6b). Note that $^{12h}CFO_{3/1}$ is the sample prepared according to the standard procedure described in the Supporting Information. Overall, Co/Fe ratio measured for $^{1h}CFO_{3/1}$ can be interpreted as a sum formula like $Co_{0.5}Fe_{0.5}OOH$. Because the resulting CFO products after 12 hours ended up onto spinel structures regardless of the ratios, a time-dependent structural evolution from the oxyhydroxide to spinel occurs. As observed in the case of $CFO_{3/1}$, the structure evolution involves an increase in the Co/Fe product ratio and, at the same time, the mass of the CFO products (see Fig. S4 for the photographs of $^{1h}CFO_{3/1}$, $^{6h}CFO_{3/1}$, and $^{12h}CFO_{3/1}$). Thus, the second formation stage should be proceeding with the continued uptake of metal cations from the reaction mixture. As both the mass of the

product and the Co/Fe ratio is increasing, there likely is a preference for the uptake of Co compared to Fe.

2.9. Magnetism study

The synthesis has yielded particles that are responsive to magnetic fields. The CFO samples generally exhibit room-temperature magnetism when interacting with magnets, but not the control samples $CFO_{Fe\text{-}free}$ and $CFO_{Co\text{-}free}$ (Fig. 7a). Quantitatively, the magnetization of $CFO_{3/1}$ is around six times higher than the control samples (Fig. S5). This shows, the homogeneous structural substitution in multinary oxides achieved via ARP, is a potential key to tune the magnetic properties of the products.

The magnetic properties of the $CFO_{3/1}$ sample obtained with varying hydrothermal synthesis times (see Section 2.8) were studied. The field-dependent magnetizations (Moment vs. H) generated from the $^{3h}CFO_{3/1}$, $^{6h}CFO_{3/1}$, and $^{12h}CFO_{3/1}$ sample are shown in Fig. 7b. These samples exhibit a relatively fast increase up to ~20000 Oe, then the gradient of the curve becomes visibly smaller but without reaching complete saturation even at 70000 Oe. At 70000 Oe, the magnetization for $^{3h}CFO_{3/1}$, $^{6h}CFO_{3/1}$, and $^{12h}CFO_{3/1}$ reaches the values of 10.0, 14.3, and 16.9 emu/g, respectively. In addition, the hysteresis loops of the three samples are clearly observed (Fig. 7c). These magnetic characteristics suggest superparamagnetic behavior for all considered samples.[56]

It is expected that the spin configurations of Fe^{III} and Co^{III} sitting in different environments, i.e. the O_h and T_d sites of a spinel structure, will affect the overall magnetic behavior of the CFO samples. Fe^{III} should have a high spin state regardless of the occupied site, whereas Co^{III} favors a high spin state in T_d sites but tends to feature a low spin state

in O_h sites. The increase of Co^{III} contents over time enhances the remanence (Fig. 7c). This suggests that the longer the time of the hydrothermal synthesis step the more T_d-sites are occupied by Co^{III}, since only high spin Co^{III}, but not low spin Co^{III} in the O_h sites, contributes to the magnetic moment.

3. Discussion

3.1. The Ferrate Route to Acidic Redox-Assisted Deposition

ARP clearly shows the excellent capability to achieve uniform distribution of Co and Fe in the binary oxide CFO in a simple manner. The oxidizing power of the metal-containing oxidant is the key to drive ARP synthesis. $KMnO_4$ represents a reasonable balance between oxidizing potentials and stability in water.[57] Good aqueous stability means great convenience in the synthesis process, while an elevated oxidizing ability enables a high reactivity and the possibility to react with a wider pool of metal ions. Due to these advantages, the usage of $KMnO_4$ for ARP of bimetallic oxides and oxyhydroxides has been established and described in our previous works. [4,14] Meanwhile, potassium chromate, for example, is discussed in the literature to be stable in water, especially in acid solution, but weak in oxidizing the more stable metal ions to perform ARP.[58]

In our preliminary studies, K_2FeO_4 has proven to be the only considered metal-containing oxidant that can form a binary metal oxide with highly inert Ni^{II}, which has not been achieved using $KMnO_4$ or $K_2Cr_2O_7$. The standard reduction potential of K_2FeO_4 is 2.20 V ,[60] while that for $KMnO_4$ is 1.509 V.[60] We have further compared the reaction for the ARP of Co^{II} with K_2FeO_4 and $KMnO_4$. For the former, the reaction rates are much

faster (see Fig. S4) and the equilibrium of the reaction shifted stronger toward the final product. Nevertheless, it should be noted that a fast reaction can also have disadvantages. A too rapid ARP process usually yields non-ordered/metastable morphologies (as shown in Fig. 2). In contrast, a relatively slow nucleation during ARP results in ordered nanostructures such as hollow spheres and Y-shaped interconnection networks.[4,25] Approaches that can slow down the redox reaction rates would be helpful in gaining novel hierarchical nanostructures for morphology-dependent applications that need multinary oxides. The high oxidizing capability of K_2FeO_4 can greatly expand the composition diversity of oxidic structures with two or more metals in the future.

3.2. Growth Mechanism of CFO

Since the CFO compositions vary with the precursor ratios, side reactions should potentially exist and compete with the redox reaction between Co^{II} and K_2FeO_4. As suggested in previous studies, K_2FeO_4 tends to undergo self-decomposition to form Fe_2O_3 by releasing oxygen:[61,62]

$$4FeO_4^{2-}(aq) + 8H^+ \rightarrow 2Fe_2O_3(s) + 3O_2 + 4H_2O \quad (3)$$

Accordingly, if Fe_2O_3 was found in the ARP products, it would indicate that the reaction rate of the side reaction in Eq. 3 can compete with the redox process between Co^{II} and K_2FeO_4 (Eq. 1). Yet, the results obtained with Raman spectroscopy, XRD and the characterization methods show that no Fe_2O_3 is formed if Co^{II} is present during the

synthesis. This means that the redox reaction between Co^{II} and K_2FeO_4 shown in Eq. 1 should be significantly faster than the self-decomposition of K_2FeO_4 (Eq. 3).

3.2.1. Formation of Inner-Sphere Reaction Intermediates

Despite the expected completeness of the reaction mentioned in Eq. 1, there is an issue with the discrepancy between the Co/Fe ratio in the synthesized CFO sample and Co/Fe in the precursors used for the synthesis. The ICP results upon prolonged time clearly shows that the Co/Fe ratio in the formed CFO never exceeds 2:1 (Fig. 6b). To explain this issue, we hypothesized a reaction mechanism in which $[Co^{II}(H_2O)_6]^{2+}$, an octahedral d^7 system, is being oxidized by $Fe^{VI}O_4^{2-}$, a tetrahedral d^2 system, prior to the material nucleation. Given that octahedral d^7 systems are generally accepted to be labile,[63] we assume that the oxidation process proceeds via the formation of a neutral inner-sphere complex of the formula $[(H_2O)_5Co^{II}\text{-}O\text{-}Fe^{VI}O_3]$, where an aqua ligand of the $[Co^{II}(H_2O)_6]^{2+}$ is substituted by a bond to one of the oxo-groups of $Fe^{VI}O_4^{2-}$ (Eq. 4a). Upon transferring one electron from the Co^{II} center to the Fe^{VI} center, one should obtain a Co^{III}-d^6 and a Fe^{V}-d^3 center (Eq. 4b).

$$[Co^{II}(H_2O)_6]^{2+} + Fe^{VI}O_4^{2-} \rightarrow [(H_2O)_5Co^{II}\text{-}O\text{-}Fe^{VI}O_3]^0 \quad (4a)$$

$$[(H_2O)_5Co^{II}\text{-}O\text{-}Fe^{VI}O_3]^0 \rightarrow [(H_2O)_5Co^{III}\text{-}O\text{-}Fe^{V}O_3]^0 \quad (4b)$$

Although the electron configurations at both metal centers do not indicate the presence of any extraordinarily stable or inert metal-ligand bonds, we assume that the inner-sphere complex will not dissociate after the redox step. The reason for this assumption is that the

formed fragments would feature charges of opposite signs, either $[Co^{III}O(H_2O)_5]^+$ and $[Fe^VO_3(H_2O)]^-$ or $[Co^{III}(H_2O)_6]^{3+}$ and $[Fe^VO_4]^{3-}$. The following redox steps are assumed to follow a similar pattern consisting of three steps: i) formation of an inner-sphere complex by substituting an aqua ligand at the Co^{II} center, ii) the transfer of one electron from Co^{II} to the Fe center, and iii) the retention of the inner-sphere complex after the reaction.

Such a mechanism should allow the redox reaction between the Fe^{VI} center and three Co^{II} centers to yield Fe^{III} and Co^{III} as observed in the experiment. However, the experimentally determined Co:Fe ratio of at most 2:1 in the synthesized CFO samples indicates that the Fe^{VI} centers likely only interact with two Co^{II} centers. We hypothesize that this is related to the charges of the reactants, as elaborated in the following. The first formation of the Co^{II}-Fe^{VI} inner-sphere complex should be benefitted by Coulomb interactions (Eq. 4a). However, the product of the first redox step is the charge-neutral Co^{III}-Fe^V complex (Eq. 4b). When this structure reacts with a second $[Co^{II}(H_2O)_6]^{2+}$ to form the positively charged Co^{III}-Fe^V-Co^{II} inner-sphere complex (Eq. 5a) for the second redox step (Eq. 5b), there is no Coulombic interaction assisting the reaction.

$$[Co^{II}(H_2O)_6]^{2+} + [(H_2O)_5Co^{III}\text{-}O\text{-}Fe^VO_3]^0 \rightarrow \{[(H_2O)_5Co^{III}\text{-}O]\text{-}Fe^VO_2\text{-}[O\text{-}(H_2O)_5Co^{II}]\}^{2+} \quad (5a)$$

$$\{[(H_2O)_5Co^{III}\text{-}O]\text{-}Fe^VO_2\text{-}[O\text{-}(H_2O)_5Co^{II}]\}^{2+} \rightarrow \{[(H_2O)_5Co^{III}\text{-}O]_2\text{-}Fe^{IV}O_2\}^{2+} \quad (5b)$$

When it comes to forming the inner-sphere complex (Eq. 6a) for the third redox step (Eq. 6b), the Coulomb interactions become hindering, as the two reactants, both $[Co^{II}(H_2O)_6]^{2+}$ and the Co^{III}-Fe^{IV}-Co^{III} complex, feature a positive charge.

$$[Co^{II}(H_2O)_6]^{2+} + \{[(H_2O)_5Co^{III}\text{-}O]_2\text{-}Fe^{IV}O_2\}^{2+} \rightarrow \{[(H_2O)_5Co^{III}\text{-}O]_2\text{-}Fe^{IV}O_2\text{-}[O\text{-}(H_2O)_5Co^{II}]\}^{4+} \quad (6a)$$

$$\{[(H_2O)_5Co^{III}\text{-}O]_2\text{-}Fe^{IV}O_2\text{-}[O\text{-}(H_2O)_5Co^{II}]\}^{4+} \rightarrow \{[(H_2O)_5Co^{III}\text{-}O]_3\text{-}Fe^{III}O_2\}^{4+} \quad (6b)$$

We speculate that the Coulomb forces make the interaction between the Fe center with a third Co^{II} unfavorable. The formation of proposed product complex of Eq 6b, $\{[(H_2O)_5Co^{III}\text{-}O]_3\text{-}Fe^{IV}O_2\}^{4+}$, should be relatively unlikely, due to the repulsion between the like charges of Co^{II} and $\{[(H_2O)_5Co^{III}\text{-}O]_2\text{-}Fe^{IV}O_2\}^{2+}$. Instead of oxidizing a third Co^{II} center, Fe would rather oxidize its oxygen-containing ligands through coupling with another highly oxidized Fe species[62,64] to reach a trivalent oxidation state, similar to the reaction in Eq. 3. Comparable electrostatic interactions are not unknown for the chemistry of FeO_4^{2-}. It has, for instance, been discussed in the literature that a positively charged Ca^{2+} ion can facilitate the reaction between two negatively charged $Fe^{VI}O_4^{2-}$ units to form O_2.[63] This may explain why the ideal stoichiometry of 3:1 in Eq. 1 cannot be achieved here.

3.2.2. Theoretical Approach Towards Inner-Sphere/Electron Transfer Reactions

To test our hypothesis, we have performed DFT calculations to obtain the reaction energies to form the inner-sphere complexes and for the electron transfer steps. The results are shown in Fig. 8. In our calculations, we assume that all metal centers feature a high-spin electron configuration. For Fe, this is justified by the tetrahedral coordination sphere. At the same time, the weakly splitting character of the aqua ligands rationalizes the assumption of a high-spin configuration for the Co centers. When the Fe and the Co centers

start to interact, the metal centers can show either ferromagnetic or antiferromagnetic coupling. Both cases have been considered, but our preliminary results for the first redox step show that the Co^{III}-Fe^{V} redox product showing anti-ferromagnetic coupling is significantly less stable than the product with ferromagnetic coupling. Thus, we only consider the reactions of the metal centers with parallel spin, similar to earlier works in literature.[61]

Fig. 8 shows, the formation of the inner-sphere complexes is, as in our hypothesis, strongly dependent on the charge of the reactants. While the Eq 4a, the formation of the first inner-sphere complex, is a strongly exothermic process with a Gibbs free energy of reaction of < -100 kJ/mol, the formation of the third inner-sphere complex is, with -13 kJ/mol, clearly less favorable. This aligns with our hypothesis and rationalizes the Co:Fe ratio in the synthesized CFO samples. Figure 8 also shows that the final redox product with three Co^{III} and one Fe^{III} is, in fact, also slightly less stable than the preceding intermediates. Although this would also be in line with the observation that each Fe only reacts with two Co centers, one should not overinterpret the results. The computational model is relatively simple and assumes that the tetrahedral coordination of the Fe center does not change during the reaction. However, Fe^{III} centers are typically found in octahedral coordination spheres, which is also the case in the synthesized CFO, as shown in the Raman spectra in Figure 4b. In other words, we may underestimate the stability of the final product by not considering the change of the coordination sphere of the Fe center. Thus, we think the main reason for never observing a Co:Fe ratio of 3:1 is related to the charges of the reactants.

3.2.3. Nucleation Stages of CFO

Both the theoretical and experimental results dictate that the proposed complex $[(H_2O)_5Co^{II}\text{-}O\text{-}Fe^{VI}O_3]^0$ likely is the key complex involved in the nucleation and particle growth. The polymerization of the complex results in the first nucleation stage. In the first hour of the nucleation (i.e., the first hour of the hydrothermal synthesis step), $[(H_2O)_5Co^{II}\text{-}O\text{-}Fe^{VI}O_3]^0$ could be the major species to assist the material growth, and thus yielding the layer of oxyhydroxide products with Co/Fe ratios close to one. As the nucleation continues to proceed, $\{[(H_2O)_5Co^{III}\text{-}O]_2\text{-}Fe^{IV}O_2\}^{2+}$ may actively participate. This results in the finding that the cobalt contents gradually increase (Co/Fe > 1, see the ICP data in Fig. 6b). It seems that the nucleation of layered oxyhydroxide favors the initiation with the zero net charge complex. In the second stage, the newly nucleated Co^{III} should be preferring the occupation of the Td sites of the spinel structure, as-suggested by the IR/Raman/magnetism data.

5. Conclusion

Our work demonstrates that K_2FeO_4 can be used as a new oxidant to conduct acidic redox-assisted precipitation (ARP) to produce cobalt iron oxides, composed of an evenly distributed mixed-metal Co-O-Fe moieties. The obtained products feature completely uniform structure substitution that surpasses the limits of that with conventional alkaline precipitation. This uniform structure substitution has been shown to stimulate adjustable magnetism, formation of vacant sites, and synergistic electrocatalytic activities.

ARP process likely features a series of inner-sphere redox-processes. This direct interaction of the different metal precursors, is a key to achieve the even distribution of the metals in the product. Eventually, ARP can be valuable to solve the still difficult production of evenly blended trinary/quaternary metal cations in a single oxide phase. K_2FeO_4 is in so

far a promising oxidant for further ARP processes, as it shows a stronger oxidizing power than all the reported oxidants. This is useful, sometimes even necessary, to drive unreactive metal species (e.g. Ni^{II}) into a multinary oxide framework. The prospects of applying ARP to design and synthesize new multinary oxide structures with unprecedented electron structures, conductivity, optical properties, and photocatalytic activities likely opens up a lot of new opportunities to deal with the future challenges of smart semiconductors. For example, our active research on preparing trinary/quaternary oxides (Co/Ni/Ce/Mn) using K_2FeO_4 has been positive, and the resultants with unique compositions clearly show interesting properties and remarkable performance.

ASSOCIATED CONTENT

Supporting Information. Experimental and Computational procedures, XRD peaks for synthesized K_2FeO_4, XPS spectra of $^{1h}CFO_{3/1}$ and $^{12h}CFO_{3/1}$ sample, XRD patterns the $CFO_{Co\text{-}free}$ and $CFO_{Fe\text{-}free}$ samples, the resultant solutions obtained by treating the precursor solution (Co/Fe ratio 3:1), and the magnetic hysteresis curves of Co_3O_4 ($CFO_{Fe\text{-}free}$) and Fe_2O_3 ($CFO_{Co\text{-}free}$) and $^{12h}CFO_{3/1}$.

The following files are available free of charge.

Supporting Information File (PDF)

AUTHOR INFORMATION

Corresponding Authors

*ccchiu@mail.nsysu.edu.tw (C.-c. Chiu)

*chunhu.chen@nsysu.edu.tw (C.-H. Chen)

Author Contributions

The manuscript was written through contributions of all authors. All authors have given approval to the final version of the manuscript.

ACKNOWLEDGMENTS

We acknowledge the financial support of the Ministry of Science and Technology (MOST) of Taiwan (Project No. MOST 109-2628-M-110-001-MY3 and the Young Scholar Fellowship Program under Project No. MOST 109-2636-M-110-004). We also thank the National Center for High-performance Computing (NCHC) for providing computational and storage resources.

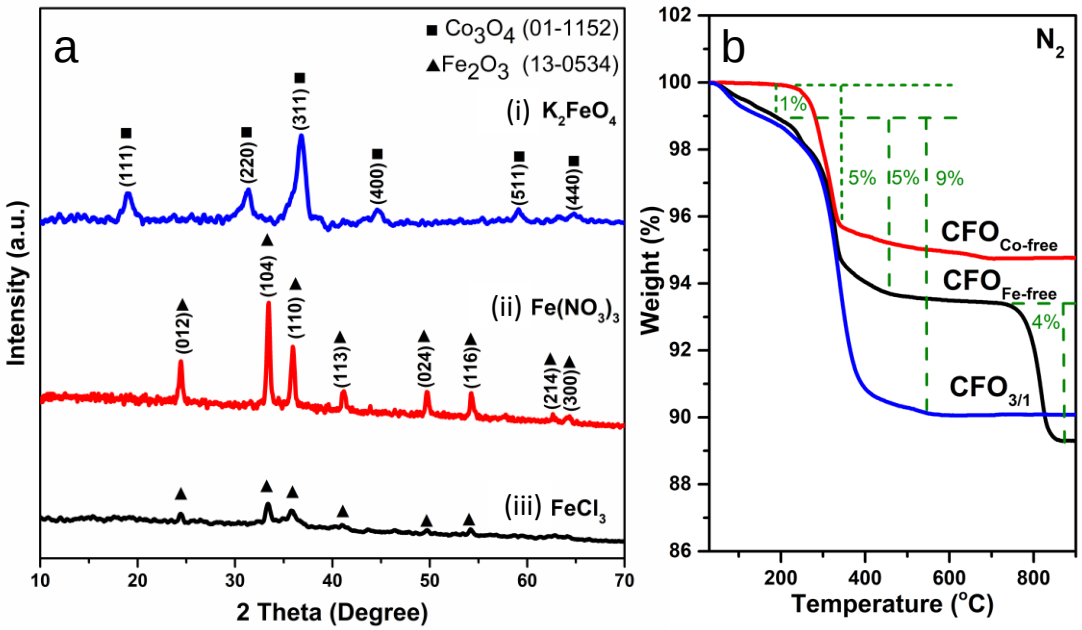

Figure 1. (a) The XRD patterns of the precipitation products obtained by reacting different iron precursors (i) $K2FeO_4$, (ii) $Fe(NO_3)_3$, and (iii) $FeCl_3$ with $Co(OAc)_2$ at a Co/Fe precursor ratio of 3:1 at 140ºC for 12 hours. (b) The TGA of $CFO_{3/1}$ compared to $CFO_{Fe\text{-}free}$ and $CFO_{Co\text{-}free}$ under inert nitrogen atmosphere.

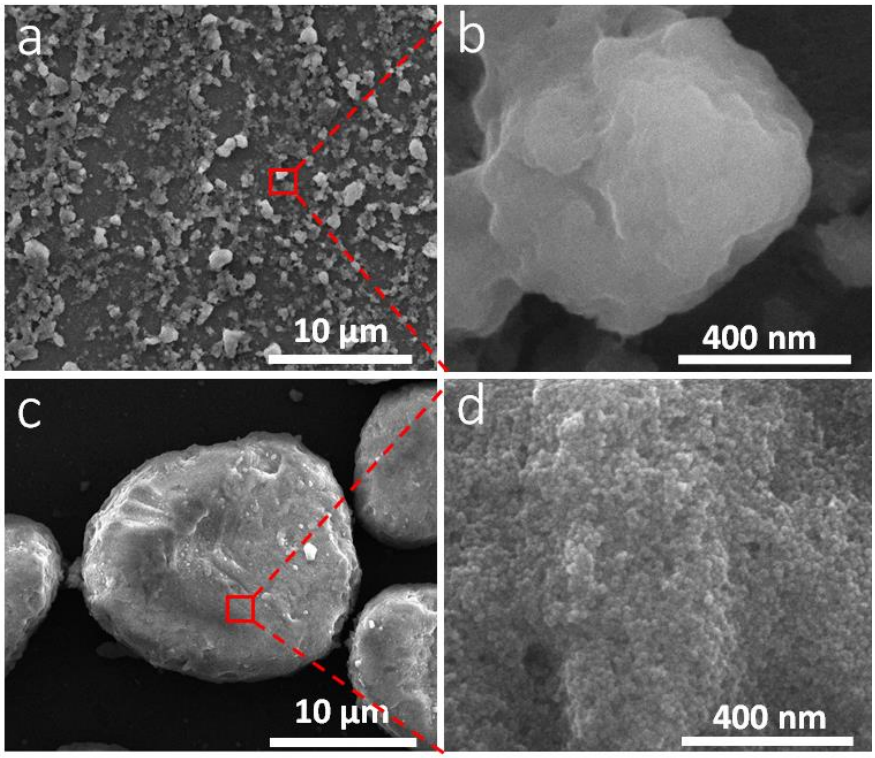

Figure 2. The SEM images of the products obtained by reacting $Co(OAc)_2$ and K_2FeO_4 at a precursor ratio of Co/Fe=3:1 at 140ºC for (a and b) 1 hour, (c and d) 12 hours.

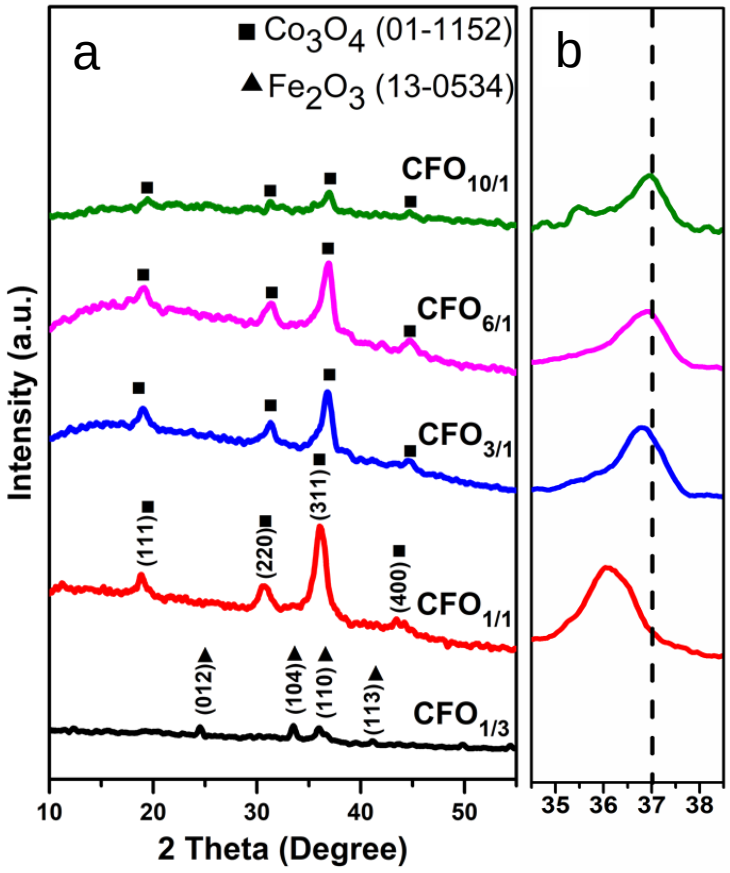

Figure 3. The XRD patterns of the products obtained by reacting $Co(OAc)_2$ with K_2FeO_4 at 140ºC for 12 hours at different precursor ratios. (a) Full spectra showing the corresponding peaks of spinel Co_3O_4. (b) A closer look at the peaks of each sample corresponding to the (311) lattice plane; the dash line corresponds to the (311) peak of pure Co_3O_4 according to JCPDS No. 01-1152.

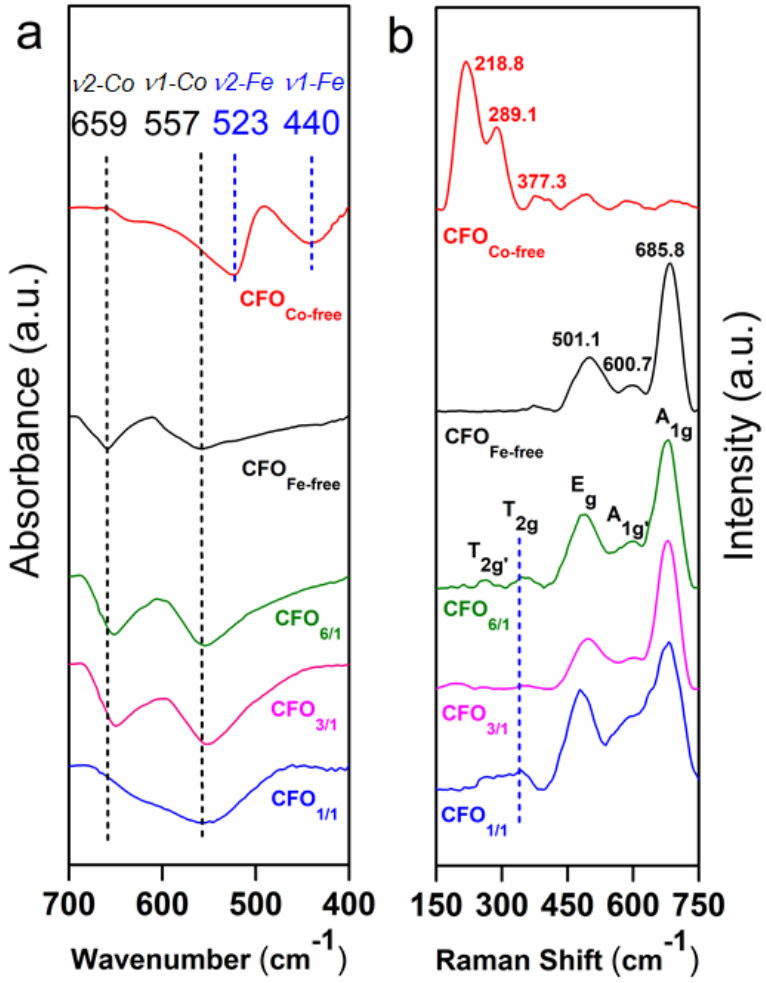

Figure 4. IR (a) and Raman spectra (b) of the CFO samples and the control samples.

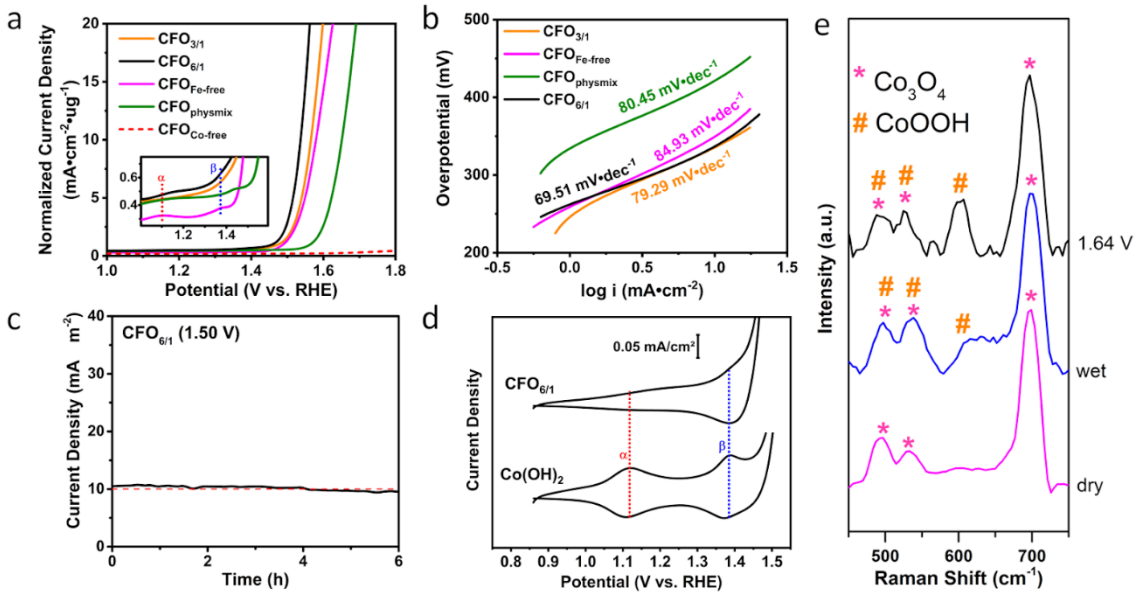

Figure 5. The electrochemical oxygen evolution activities of different CFO samples measured under 1.0 M Fe-free KOH electrolyte12 h. (a) The linear scan voltammetry curves of the CFO samples compared with the control samples: Co_3O_4 ($CFO_{Fe\text{-}free}$), Fe_2O_3 ($CFO_{Co\text{-}free}$, graphed against current density for reference), and a physical mixture ($CFO_{physmix}$) comprised of these two control samples, whose Co/Fe mole ratio matches the ICP result of $CFO_{3/1}$. All current densities were normalized using the mass (μg) percentage of Co in the samples, except Fe_2O_3. The inset shows the pre-onset $Co^{II/III}$ (peak α) and $Co^{III/IV}$ (peak β) transitions. (b) Tafel plots of the CFO and control samples. (c) Stability performance of $CFO_{6/1}$ at 1.50 V for 6 hours. The red-dashed, horizontal line is a guide for the 10 mA•cm^{-1} mark. (d) The cyclic voltammetry curves of $CFO_{6/1}$ and $Co(OH)_2$ highlighting the absence of the $Co^{II/III}$ peaks in $CFO_{6/1}$. The $Co^{III/IV}$ transition of $CFO_{6/1}$ goes alongside the OER onset. (e) Raman spectra of the $CFO_{6/1}$ sample before (dry) and after (wet) immersion in 1 M KOH solution, and under OER operation at 1.64 V.

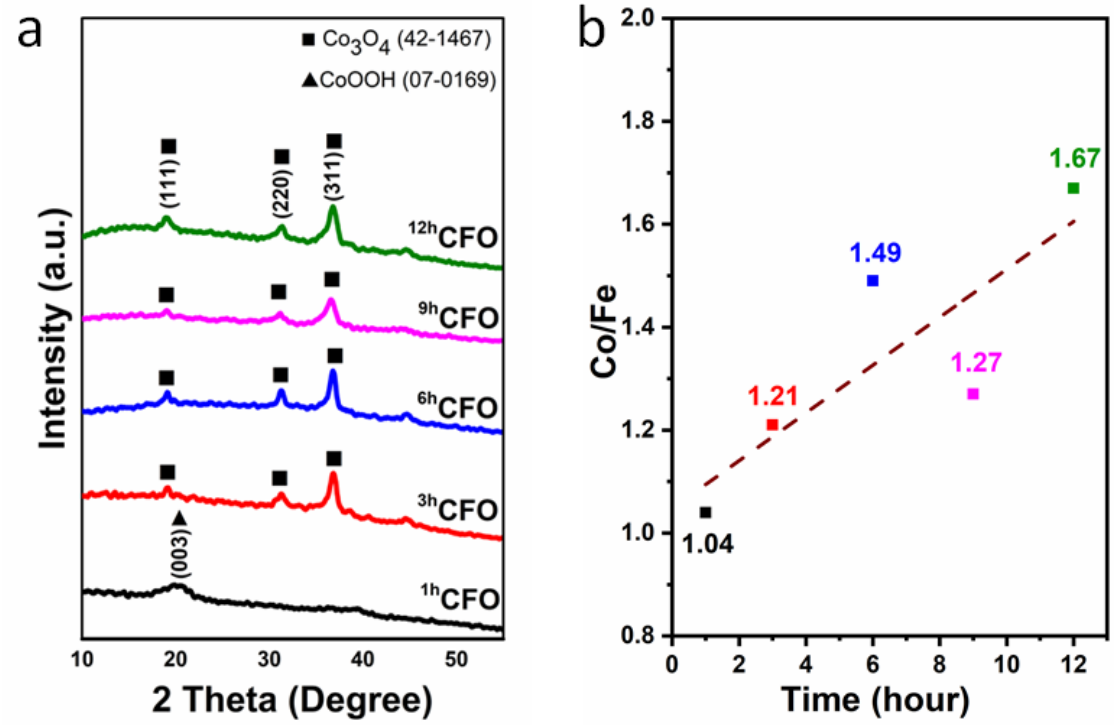

Figure 6. (a) The XRD patterns of $CFO_{3/1}$ samples prepared by conducting the hydrothermal synthesis step at 140ºC for varying lengths of time. (b) The Co/Fe ratios of the $CFO_{3/1}$ samples prepared by conducting the hydrothermal synthesis step at 140ºC for varying lengths of time. The dash-line trend shows a gradual increase of the Co/Fe ratios over the period.

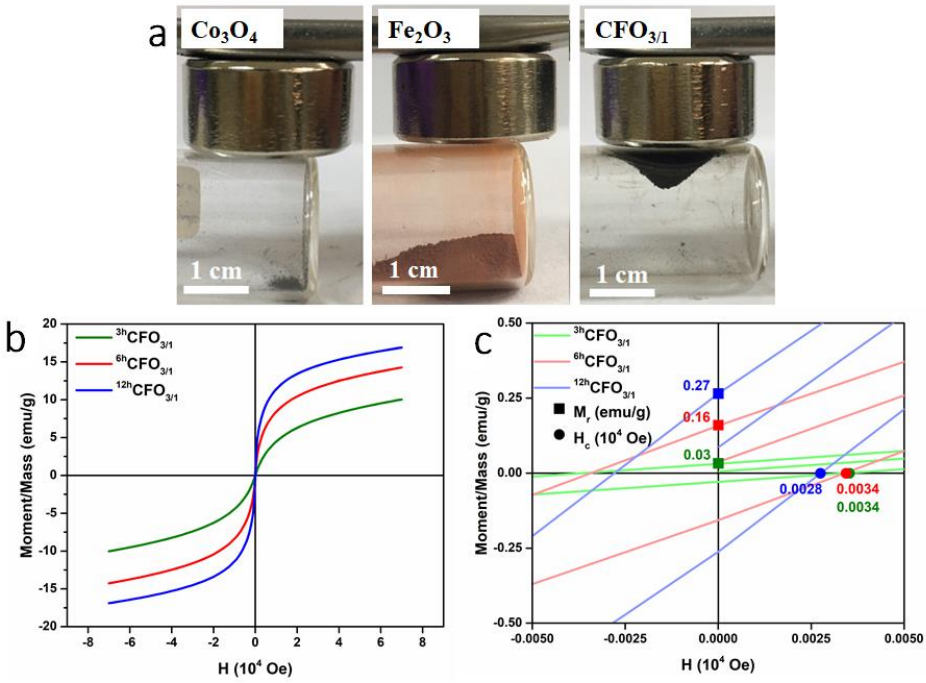

Figure 7. The magnetic study of the CFO and control samples. (a) The magnet-attraction tests at room temperature on Co_3O_4 ($CFO_{Fe\text{-}free}$), Fe_2O_3 ($CFO_{Co\text{-}free}$), and $CFO_{3/1}$. (b) The comparison of the magnetic hysteresis curves of the CFO samples prepared with hydrothermal synthesis steps of varying lengths of time. (c) A magnified view of (b), showing the magnetic remanence (M_r, square dots) and coercivity (H_c, round dots) values. The measurements in (b) and (c) were conducted at 300 K.

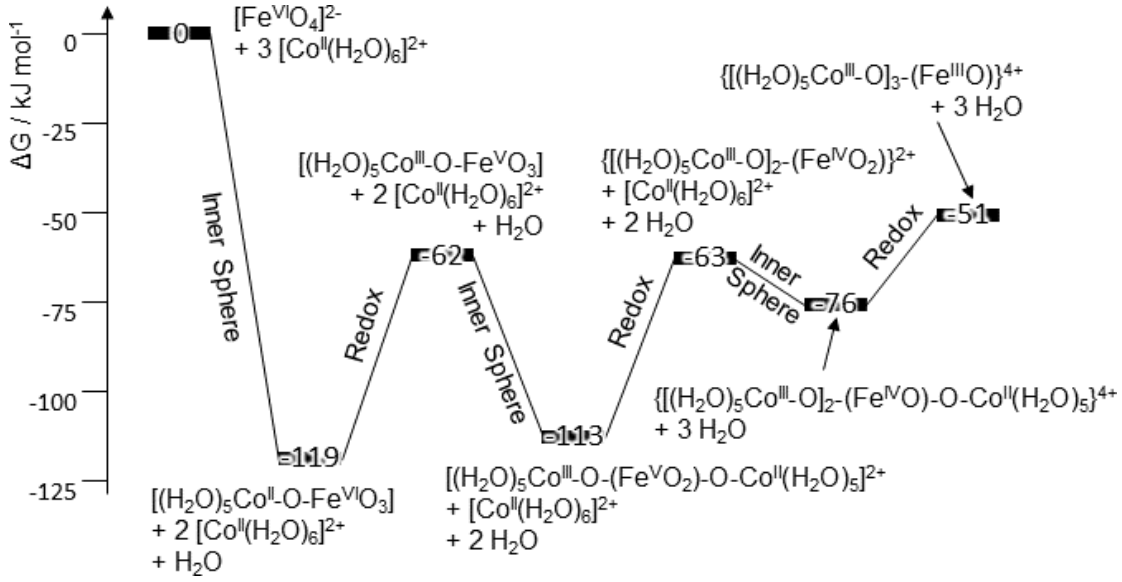

Figure 8. The calculated Gibbs free energies for the proposed redox reaction of $Fe^{IV}O_4^{2-}$ with three $[Co^{II}(H_2O)_6]^{2+}$ via the formation of inner-sphere complexes. For the calculations, it has been assumed that the metal centers show ferromagnetic coupling.

Table 1. The conductivity of the CFO and control samples. All the samples were prepared via a hydrothermal synthesis step at 140°C for 1 hour and also 12-hour samples.

Sample	Sheet resistance (Ω/□)
Cobalt oxide ($^{1h}CFO_{Fe\text{-}free}$)	$1.69 \pm 0.35 \times 10^{3}$
Iron oxide ($^{1h}CFO_{Co\text{-}free}$)	$6.45 \pm 0.86 \times 10^{6}$
[a]Physical mixture of $^{1h}CFO_{Fe\text{-}free}$ and $^{1h}CFO_{Co\text{-}free}$	$1.20 \pm 0.11 \times 10^{3}$
$^{1h}CFO_{3/1}$	$4.40 \pm 0.89 \times 10^{2}$
$^{12h}CFO_{3/1}$	$3.00 \pm 0.63 \times 10^{2}$

[a] Co/Fe ratio of 3/1

References

(1) Szot, K.; Speier, W.; Bihlmayer, G.; Waser, R. Switching the Electrical Resistance of Individual Dislocations in Single-Crystalline $SrTiO_3$. *Nat. Mater.* **2006,** *5*, 312-320.

(2) Sarkar, A.; Velasco, L.; Wang, D.; Wang, Q.; Talasila, G.; de Biasi, L.; Kübel, C.; Brezesinski, T.; Bhattacharya, S. S.; Hahn, H.; Breitung, B. High Entropy Oxides for Reversible Energy Storage. *Nat. Commun.* **2018,** *9*, 3400.

(3) Zhang, B.; Zheng, X.; Voznyy, O.; Comin, R.; Bajdich, M.; García-Melchor, M.; Han, L.; Xu, J.; Liu, M.; Zheng, L.; García de Arquer, F. P.; Dinh, C. T.; Fan, F.; Yuan, M.; Yassitepe, E.; Chen, N.; Regier, T.; Liu, P.; Li, Y.; De Luna, P.; Janmohamed, A.; Xin, H. L.; Yang, H.; Vojvodic, A.; Sargent, E. H. Homogeneously Dispersed Multimetal Oxygen-Evolving Catalysts. *Science* **2016,** *352*, 333-337.

(4) Lan, W.-J.; Kuo, C.-C.; Chen, C.-H. Hierarchical Nanostructures with Unique Y-Shaped Interconnection Networks in Manganese Substituted Cobalt Oxides: The Enhancement Effect in Electrochemical Sensing Performance. *Chem. Commun.* **2013,** *49*, 3025-3027.

(5) Guo, T.; Yao, M.-S.; Lin, Y.-H.; Nan, C.-W. A Comprehensive Review on Synthesis Methods for Transition-Metal Oxide Nanostructures. *CrystEngComm* **2015,** *17*, 3551-3585.

(6) Rios, E.; Gautier, J. L.; Poillerat, G.; Chartier, P. Mixed Valency Spinel Oxides of Transition Metals and Electrocatalysis: Case of The $Mn_xCo_{3-x}O_4$ System. *Electrochim. Acta* **1998,** *44*, 1491-1497.

(7) Kuznetsov, D. A.; Han, B.; Yu, Y.; Rao, R. R.; Hwang, J.; Román-Leshkov, Y.; Shao-Horn, Y. Tuning Redox Transitions via Inductive Effect in Metal Oxides and Complexes, and Implications in Oxygen Electrocatalysis. *Joule* **2018,** *2*, 225-244.

(8) Yamada, Y.; Tsung, C.-K.; Huang, W.; Huo, Z.; Habas, S. E.; Soejima, T.; Aliaga, C. E.; Somorjai, G. A.; Yang, P. Nanocrystal Bilayer for Tandem Catalysis. *Nat. Chem.* **2011,** *3*, 372-376.

(9) Wang, S.; Zhang, L.; Zhang, W.; Wang, P.; Qin, Z.; Yan, W.; Dong, M.; Li, J.; Wang, J.; He, L.; Olsbye, U.; Fan, W. Selective Conversion of CO_2 into Propene and Butene. *Chem* **2020,** *6*, 3344-3363.

(10) Zecevic, J.; Vanbutsele, G.; de Jong, K. P.; Martens, J. A. Nanoscale Intimacy in Bifunctional Catalysts for Selective Conversion of Hydrocarbons. *Nature* **2015,** *528*, 245-248.

(11) Huang, W.; Zhang, J.; Liu, D.; Xu, W.; Wang, Y.; Yao, J.; Tan, H. T.; Dinh, K. N.; Wu, C.; Kuang, M.; Fang, W.; Dangol, R.; Song, L.; Zhou, K.; Liu, C.; Xu, J. W.; Liu, B.; Yan, Q. Tuning the Electronic Structures of Multimetal Oxide Nanoplates to Realize Favorable Adsorption Energies of Oxygenated Intermediates. *ACS Nano* **2020,** *14*, 17640-17651.

(12) Qiu, H.-J.; Fang, G.; Gao, J.; Wen, Y.; Lv, J.; Li, H.; Xie, G.; Liu, X.; Sun, S. Noble Metal-Free Nanoporous High-Entropy Alloys as Highly Efficient Electrocatalysts for Oxygen Evolution Reaction. *ACS Mater. Lett.* **2019,** *1*, 526-533.

(13) Shriver, D.; Weller, M.; Overton, T.; Rourke, J.; Armstrong, F. Materials Chemistry and Nanomaterials. In *Inorganic Chemistry*, 6th Ed.; W. H. Freeman and Company, 2014; pp. 655-727.

(14) Kuo, C.-C.; Lan, W.-J.; Chen, C.-H. Redox Preparation of Mixed-Valence Cobalt Manganese Oxide Nanostructured Materials: Highly Efficient Noble Metal-Free Electrocatalysts for Sensing Hydrogen Peroxide. *Nanoscale* **2014,** *6*, 334-341.
(15) Yang, R.; Mei, C.; Wu, X.; Yu, X.; Shi, Z. Mn–Cu Binary Metal Oxides with Molecular-Scale Homogeneity for Hg^0 Removal from Coal-Fired Flue Gas. *Ind. Eng. Chem. Res.* **2019,** *58*, 19292-19301.
(16) Hu, X.; Huang, L.; Zhang, J.; Li, H.; Zha, K.; Shi, L.; Zhang, D. Facile and Template-Free Fabrication of Mesoporous 3D Nanosphere-like $Mn_xCo_{3-x}O_4$ as Highly Effective Catalysts for Low Temperature SCR of NO_x with NH_3. *J. Mater. Chem. A* **2018,** *6*, 2952-2963.
(17) Ray, C.; Dutta, S.; Roy, A.; Sahoo, R.; Pal, T. Redox Mediated Synthesis of Hierarchical Bi_2O_3/MnO_2 Nanoflowers: A Non-Enzymatic Hydrogen Peroxide Electrochemical Sensor. *Dalton Trans.* **2016,** *45*, 4780-4790.
(18) Chen, C. H.; Njagi, E. C.; Chen, S. Y.; Horvath, D. T.; Xu, L.; Morey, A.; Mackin, C.; Joesten, R.; Suib, S. L. Structural Distortion of Molybdenum-Doped Manganese Oxide Octahedral Molecular Sieves for Enhanced Catalytic Performance. *Inorg. Chem.* **2015,** *54*, 10163-10171.
(19) Yang, S.; Zhao, H.; Dong, F.; Tang, Z.; Zha, F. Three-Dimensional Flower-Like OMS-2 Supported Ru Catalysts for Application in The Combustion Reaction of *O*-Dichlorobenzene. *Catal. Sci. Technol.* **2019,** *9*, 6503-6516.
(20) Chen, J.; Yan, D.; Xu, Z.; Chen, X.; Chen, X.; Xu, W.; Jia, H.; Chen, J. A Novel Redox Precipitation to Synthesize Au-Doped α-MnO_2 with High Dispersion toward Low-Temperature Oxidation of Formaldehyde. *Environ. Sci. Technol.* **2018,** *52*, 4728-4737.
(21) Chen, X.; Shen, Y.-F.; Suib, S. L.; O'Young, C. L. Characterization of Manganese Oxide Octahedral Molecular Sieve (M−OMS-2) Materials with Different Metal Cation Dopants. *Chem. Mater.* **2002,** *14*, 940-948.
(22) Yuan, J.; Li, W.-N.; Gomez, S.; Suib, S. L. Shape-Controlled Synthesis of Manganese Oxide Octahedral Molecular Sieve Three-Dimensional Nanostructures. *J. Am. Chem. Soc.* **2005,** *127*, 14184-14185.
(23) Li, W.-N.; Yuan, J.; Gomez-Mower, S.; Sithambaram, S.; Suib, S. L. Synthesis of Single Crystal Manganese Oxide Octahedral Molecular Sieve (OMS) Nanostructures with Tunable Tunnels and Shapes. *J. Phys. Chem. B* **2006,** *110*, 3066-3070.
(24) Li, W.-N.; Yuan, J.; Shen, X.-F.; Gomez-Mower, S.; Xu, L.-P.; Sithambaram, S.; Aindow, M.; Suib, S. L. Hydrothermal Synthesis of Structure- and Shape-Controlled Manganese Oxide Octahedral Molecular Sieve Nanomaterials. *Adv. Funct. Mater.* **2006,** *16*, 1247-1253.
(25) Chen, C.-H.; Abbas, S. F.; Morey, A.; Sithambaram, S.; Xu, L.-P.; Garces, H. F.; Hines, W. A.; Suib, S. L. Controlled Synthesis of Self-Assembled Metal Oxide Hollow Spheres Via Tuning Redox Potentials: Versatile Nanostructured Cobalt Oxides. *Adv. Mater.* **2008,** *20*, 1205-1209.
(26) King'ondu, C. K.; Opembe, N.; Chen, C.-h.; Ngala, K.; Huang, H.; Iyer, A.; Garcés, H. F.; Suib, S. L. Manganese Oxide Octahedral Molecular Sieves (OMS-2) Multiple Framework Substitutions: A New Route to OMS-2 Particle Size and Morphology Control. *Adv. Funct. Mater.* **2011,** *21*, 312-323.

(27) Zeng, X.; Li, B.; Liu, R.; Li, X.; Zhu, T. Investigation of Promotion Effect of Cu Doped MnO_2 Catalysts on Ketone-Type VOCs Degradation in a One-Stage Plasma-Catalysis System. *Chem. Eng. J.* **2020,** *384*, 123362.
(28) Yin, Y.-G.; Xu, W.-Q.; Suib, S. L.; O'Young, C. L. Lattice Oxygen Mobility and Structural Stability of Ni and Cu Octahedral Molecular Sieves Having The Cryptomelane Structure. *Inorg. Chem.* **1995,** *34*, 4187-4193.
(29) Ren, Z.; Wu, Z.; Song, W.; Xiao, W.; Guo, Y.; Ding, J.; Suib, S. L.; Gao, P.-X. Low Temperature Propane Oxidation over Co_3O_4 Based Nano-Array Catalysts: Ni Dopant Effect, Reaction Mechanism And Structural Stability. *Appl. Catal. B-Environ.* **2016,** *180*, 150-160.
(30) Yang, Y.; Huang, J.; Zhang, S.; Wang, S.; Deng, S.; Wang, B.; Yu, G. Catalytic Removal of Gaseous HCBz on Cu Doped OMS: Effect of Cu Location on Catalytic Performance. *Appl. Catal. B-Environ.* **2014,** *150-151*, 167-178.
(31) Jiang, Y.; Cheng, G.; Yang, R.; Liu, H.; Sun, M.; Yu, L.; Hao, Z. Influence of Preparation Temperature and Acid Treatment on the Catalytic Activity of MnO_2. *J. Solid State Chem.* **2019,** *272*, 173-181.
(32) Yang, J.; Liu, H.; Martens, W. N.; Frost, R. L. Synthesis and Characterization of Cobalt Hydroxide, Cobalt Oxyhydroxide, and Cobalt Oxide Nanodiscs. *J. Phys. Chem. C* **2010,** *114*, 111-119.
(33) Zhou, Z.; Zhang, Y.; Wang, Z.; Wei, W.; Tang, W.; Shi, J.; Xiong, R. Electronic Structure Studies of the Spinel $CoFe_2O_4$ by X-Ray Photoelectron Spectroscopy. *Appl. Surf. Sci.* **2008,** *254*, 6972-6975.
(34) Zhao, Q.; Fu, L.; Jiang, D.; Ouyang, J.; Hu, Y.; Yang, H.; Xi, Y. Nanoclay-Modulated Oxygen Vacancies of Metal Oxide. *Commun. Chem.* **2019,** *2*, 11.
(35) Wang, Z.; Wang, W.; Zhang, L.; Jiang, D. Surface Oxygen Vacancies on Co_3O_4 Mediated Catalytic Formaldehyde Oxidation at Room Temperature. *Catal. Sci. Technol.* **2016,** *6*, 3845-3853.
(36) Liao, P.-C.; Jhang, R.-H.; Chiu, Y.-H.; Valinton, J. A. A.; Yeh, C.-H.; Ebajo, V. D.; Wang, C.-H.; Chen, C.-H. Rock Salt Oxide Hollow Spheres Achieving Durable Performance in Bifunctional Oxygen Energy Cells. *ACS Appl. Energy Mater.* **2021,** *4*, 3448-3459.
(37) Dippong, T.; Levei, E. A.; Borodi, G.; Goga, F.; Barbu Tudoran, L. Influence of Co/Fe Ratio on The Oxide Phases in Nanoparticles of $Co_xFe_{3-x}O_4$. *J. Therm. Anal. Calorim.* **2015,** *119*, 1001-1009.
(38) Bahlawane, N.; Ngamou, P. H. T.; Vannier, V.; Kottke, T.; Heberle, J.; Kohse-Höinghaus, K. Tailoring the Properties and the Reactivity of the Spinel Cobalt Oxide. *Phys. Chem. Chem. Phys.* **2009,** *11*, 9224-9232.
(39) He, X.; Zhao, Y.; Chen, R.; Zhang, H.; Liu, J.; Liu, Q.; Song, D.; Li, R.; Wang, J. Hierarchical $FeCo_2O_4$@polypyrrole Core/Shell Nanowires on Carbon Cloth for High-Performance Flexible All-Solid-State Asymmetric Supercapacitors. *ACS Sustain. Chem. Eng.* **2018,** *6*, 14945-14954.

(40) Hao, C.; Shen, Y.; Wang, Z.; Wang, X.; Feng, F.; Ge, C.; Zhao, Y.; Wang, K. Preparation and Characterization of Fe_2O_3 Nanoparticles by Solid-Phase Method and Its Hydrogen Peroxide Sensing Properties. *ACS Sustain. Chem. Eng.* **2016,** *4*, 1069-1077.
(41) Wang, S.; Wang, R.; Chang, J.; Hu, N.; Xu, C. Self-Supporting Co_3O_4/Graphene Hybrid Films as Binder-Free Anode Materials for Lithium Ion Batteries. *Sci. Rep.* **2018,** *8*, 3182.
(42) Varghese, S.; Cutrufello, M. G.; Rombi, E.; Monaci, R.; Cannas, C.; Ferino, I. Mesoporous Hard-Templated Me–Co [Me = Cu, Fe] Spinel Oxides for Water Gas Shift Reaction. *J. Porous Mater.* **2014,** *21*, 539-549.
(43) Liu, X.; Wang, L.; Yu, P.; Tian, C.; Sun, F.; Ma, J.; Li, W.; Fu, H. A Stable Bifunctional Catalyst for Rechargeable Zinc-Air Batteries: Iron-Cobalt Nanoparticles Embedded in a Nitrogen-Doped 3D Carbon Matrix. *Angew. Chem., Int. Ed.* **2018,** *57*, 16166-16170.
(44) Suarez, J.; Daboin, V.; Gonzalez, G.; Briceno, S. Chitosan-Polyvinylpyrrolidone $Co_xFe_{3-x}O_4$ ($0.25 \leq x \leq 1$) Nanoparticles for Hyperthermia Applications. *Int. J. Biol. Macromol.* **2020,** *164*, 3403-3410.
(45) Foerster, M.; Iliev, M.; Dix, N.; Martí, X.; Barchuk, M.; Sánchez, F.; Fontcuberta, J. The Poisson Ratio in $CoFe_2O_4$ Spinel Thin Films. *Adv. Funct. Mater.* **2012,** *22*, 4344-4351.
(46) Rivas-Murias, B.; Salgueiriño, V. Thermodynamic CoO–Co_3O_4 Crossover using Raman Spectroscopy in Magnetic Octahedron-Shaped Nanocrystals. *J. Raman Spectrosc.* **2017,** *48*, 837-841.
(47) Chandramohan, P.; Srinivasan, M. P.; Velmurugan, S.; Narasimhan, S. V. Cation Distribution and Particle Size Effect on Raman Spectrum of $CoFe_2O_4$. *J. Solid State Chem.* **2011,** *184*, 89-96.
(48) Burke, M. S.; Kast, M. G.; Trotochaud, L.; Smith, A. M.; Boettcher, S. W. Cobalt–Iron (Oxy)hydroxide Oxygen Evolution Electrocatalysts: The Role of Structure and Composition on Activity, Stability, and Mechanism. *J. Am. Chem. Soc.* **2015,** *137*, 3638-3648.
(49) Li, Y.; Li, F.-M.; Meng, X.-Y.; Li, S.-N.; Zeng, J.-H.; Chen, Y. Ultrathin Co_3O_4 Nanomeshes for the Oxygen Evolution Reaction. *ACS Catal.* **2018,** *8*, 1913-1920.
(50) Zhou, J.; Zhang, L.; Huang, Y.-C.; Dong, C.-L.; Lin, H.-J.; Chen, C.-T.; Tjeng, L. H.; Hu, Z. Voltage- And Time-Dependent Valence State Transition in Cobalt Oxide Catalysts During the Oxygen Evolution Reaction. *Nat. Commun.* **2020,** *11*, 1984.
(51) Zhu, Y.; Kuo, T.-R.; Li, Y.-H.; Qi, M.-Y.; Chen, H. Wang, J.; Xu, Y.-J.; Chen, H. M. Emerging Dynamic Structure of Electrocatalysts Unveiled by *In Situ* X-ray Diffraction/Absorption Spectroscopy. *Energy Environ. Sci.* **2021**, *14*, 1928-1958.
(52) Zhu, Y.; Wang, J.; Chu, H.; Chu, Y.-C. and Chen, H. M. In Situ/Operando Studies for Designing Next-Generation Electrocatalysts. *ACS Energy Lett*. 2020, *5*, 1281-1291.
(53) Moysiadou, A.; Lee, S.; Hsu, C.-S.; Chen, H. M.; Hu, X. Mechanism of Oxygen Evolution Catalyzed by Cobalt Oxyhydroxide: Cobalt Superoxide Species as a Key Intermediate and Dioxygen Release as a Rate-Determining Step. *J. Am. Chem. Soc*. **2020**, *142*, 11901-11914.
(54) Pasquini, C.; D'Amario, L.; Zaharieva, I.; Dau, H. Operando Raman Spectroscopy Tracks Oxidation-State Changes in an Amorphous Co Oxide Material for Electrocatalysis of the Oxygen Evolution Reaction. *J. Chem. Phys*. **2020**, *152*, 194202.

(55) Yang, J.; Liu, H.; Martens, W. N. Frost, R. L. Synthesis and Characterization of Cobalt Hydroxide, Cobalt Oxyhydroxide, and Cobalt Oxide Nanodiscs. *J. Phys. Chem. C* **2010**, *114*, 111–119
(56) Pardo, A.; Gómez-Florit, M.; Barbosa, S.; Taboada, P.; Domingues, R. M. A.; Gomes, M. E. Magnetic Nanocomposite Hydrogels for Tissue Engineering: Design Concepts and Remote Actuation Strategies to Control Cell Fate. *ACS Nano* **2021,** *15*, 175-209.
(57) Rees, T. The Stability of Potassium Permanganate Solutions. *J. Chem. Educ.* **1987,** *64*, 1058.
(58) Pietrzyk, D. J.; Frank, C. W. Oxidizing and Reducing Agents as Titrants in Analytical Chemistry. In *Analytical Chemistry*; Academic Press, 1979; pp 265-290.
(59) Wood, R. H. The Heat, Free Energy and Entropy of the Ferrate(VI) Ion. *J. Am. Chem. Soc.* **1958,** *80*, 2038-2041.
(60) Hugus, Z. Z.; Latimer, W. M. The Heat of Oxidation of Manganous Ion to Permanganate and the Manganese Potentials. *J. Electrochem. Soc.* **1951,** *98*, 296-298.
(61) Licht, S.; Wang, B.; Ghosh, S. Energetic Iron(VI) Chemistry: The Super-Iron Battery. *Science* **1999,** *285*, 1039-1042.
(62) Lee, Y.; Kissner, R.; von Gunten, U. Reaction of Ferrate(VI) with ABTS and Self-Decay of Ferrate(VI): Kinetics and Mechanisms. *Environ. Sci. Technol.* **2014,** *48*, 5154-5162.
(63) Miessler, G. L.; Tarr, D. A. Coordination Chemistry IV: Reactions and Mechanisms. In *Inorganic Chemistry*, 5th Ed.; Pearson, 2014; pp. 437-474.
(64) Ma, L.; Lam, W. W.; Lo, P. K.; Lau, K. C.; Lau, T. C. Ca^{2+}-Induced Oxygen Generation by FeO_4^{2-} at pH 9-10. *Angew. Chem., Int. Ed.* **2016,** *55*, 3012-3016.